Plasma soup for the pyrometallurgist's soul

by Q.G. Reynolds[1,2], B. Bowman[3], M.W. Erwee[4], I.J. Geldenhuys[2,5], C. Sandrock[6], G.A. Venter[7], B.S. Xakalashe[1], J. Zietsman[8,9]

Affiliation:
[1]Pyrometallurgy Division, Mintek, South Africa
[2]Department of Chemical Engineering, Stellenbosch University, South Africa
[3]Independent Consultant, USA
[4]Samancor Chrome Ltd, South Africa
[5]Independent Consultant, South Africa
[6]Independent Consultant, South Africa
[7]Department of Chemistry, University of Cape Town, South Africa
[8]Ex Mente Technologies, South Africa
[9]Department of Metallurgical Engineering, University of Pretoria, South Africa

Correspondence to:
Q.G. Reynolds

Email:
QuinnR@mintek.co.za

Dates:
Received: 22 Oct. 2024
Published: March 2025

How to cite:
Reynolds, Q.G., Bowman, B., Erwee, M.W., Geldenhuys, I.J., Sandrock, C., Venter, G.A., Xakalashe, B.S., Zietsman, J. 2025. Plasma soup for the pyrometallurgist's soul. *Journal of the Southern African Institute of Mining and Metallurgy*, vol. 125, no. 3, pp. 129–144

DOI ID:
https://doi.org/10.17159/2411-9717/758/2025

ORCiD:
Q.G. Reynolds
http://orcid.org/0000-0002-5196-8586

This paper is based on a presentation given at the Mintek@90 Conference 2024, 11-12 November 2024, Sandton Convention Centre, Johannesburg, South Africa

Abstract

Understanding the behaviour of plasma arcs is an important part of the design and operation of direct current electric arc furnace smelting processes, which are used in the industrial production of many metallurgical commodities. In recent years numerical and computational modelling techniques have begun to illuminate the complexity of arc behaviour and how it is deeply connected to the thermodynamic and physical properties of the arc plasma. Plasma properties may be estimated from first principles using statistical mechanics methods, but this requires as input some knowledge of the composition of the gas phase that occurs over the process during smelting. In this paper the authors describe a workflow using thermochemistry software to predict the expected gas phase composition through a given process, followed by plasma property calculations using an open-source software tool that has been in development for several years. This tool, 'minplascalc' has been in development for several years and is also described in detail here. The workflow is then applied to the calculation of plasma properties of interest for a variety of historical and current pyrometallurgical processes, and the results are compared. The plasma property data are published in an open-access database for general use.

Keywords

plasma, arc furnace, simulation, Mmaterial properties, software

Introduction

Over the past five decades Mintek has conducted extensive applied research into a wide range of pyrometallurgical processes using direct current (DC) electric arc furnace technology. Many of these processes have been successfully developed through to large pilot-plant or industrial scales and include commodities such as ferrochromium, ferronickel, high-titania slag, zinc, magnesium, cobalt, and platinum group metals (Barcza, 1986; Jones, Curr, 2006).

As shown in Figure 1, DC arc furnaces consist of a cylindrical refractory-lined vessel, which is used to contain the molten process products, which are typically immiscible slag (metal oxide) and alloy phases at temperatures in excess of 1400°C. Raw material, fluxes, and reductants are introduced through feedports in the furnace roof, with the feed rate carefully controlled to match the power input in order to maintain an open bath surface. The furnace is usually operated in semi-batch mode, with continuous feed and periodic removal of products by tapping. Power is supplied to the unit from a transformer and rectifier combination – one or more graphite electrodes enter through the roof of the vessel, and the electrical circuit is completed either through a hearth anode in the base of the furnace or, less commonly, between anode and cathode electrodes.

The plasma arc, which gives the furnace its name bridges the gap between the tip of the electrode and the molten bath surface (see Figure 2). The arc acts as the engine room of the furnace, driving intense transfer of thermal and mechanical energy to the metallurgical process. Understanding and managing the arc is an important aspect in the successful running of any DC arc furnace plant (Geldenhuys, 2017).

Arcs are formed from process gases in the freeboard, which have been heated to the point that they decompose into a mixture of molecules, atoms, charged ions, and electrons – a plasma. This 'plasma soup' renders the arc electrically conductive, and powerful coupling between the electric, magnetic, thermal, and momentum fields shapes the arc into a high temperature, high velocity jet, which can reach tens of thousands of Kelvin and travel at kilometres per second (Bowman, Krüger, 2009).

Like any good soup, changing the ingredients can have an effect on the properties of the final result, ranging from subtle to strong; likewise, the composition of the freeboard gases over different metallurgical processes influences the electrical and thermal behaviour of the resulting arc.

Experimental studies on plasma arcs in situ are very challenging due to the extreme conditions inside operating furnaces. Due to this, the development of mathematical and numerical models of arc

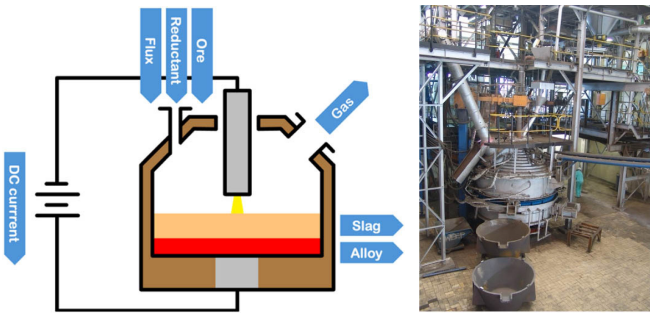

Figure 1—(*l*) Schematic of a typical DC arc furnace, (*r*) photograph of a 5.6 MVA pilot furnace ©Mintek 2007

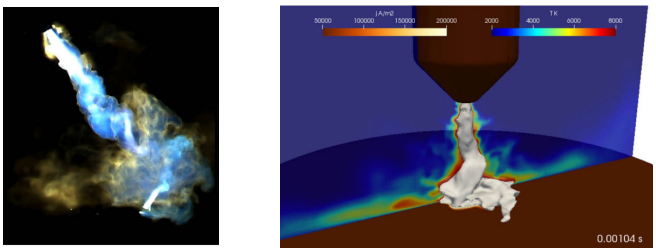

Figure 2—(*l*) Photograph of DC plasma arc in air at 2 kA and 20 cm arc length ©Mintek 2015, (*r*) computational multiphysics model of a DC arc at 1 kA and 10 cm length (Reynolds, 2018)

behaviour has been an important aspect of research in this area for many years, and measurements must often be supplemented with such models to improve the understanding of arc behaviour and generate useful insight. Models fall into a range of categories from lumped parameter steady-state or dynamic approaches such as Bowman's empirical models for DC and Cassie-Mayr models for AC, through to more complex 1D dynamic formulations such as channel arc models, and finally up to 2D and 3D spatial magnetohydrodynamic models, which directly simulate the electromagnetic, temperature, and velocity fields from the fundamental governing equations. The pros and cons of different models are well documented in (Bowman, Krüger, 2009) and (Haraldsson et al., 2021).

All arc modelling requires input information about the thermodynamic, transport, and radiation properties of the plasma material for the problem in question. These are sometimes simply bulk-averaged values of properties like electrical conductivity, but particularly in more sophisticated models detailed knowledge of the dependence of properties on plasma temperature and pressure is also needed. Direct measurement of plasma properties is again extremely difficult even in controlled laboratory conditions, but it is possible to calculate them from first principles using methods from branches of physics such as statistical mechanics. These calculations are very complex and tedious, and their implementation is non-trivial. Results of some such calculations have previously been published for materials such as pure noble gases, simple gases such as pure hydrogen, and selected binary mixtures such as Ar-H_2 and CO_2-Cu (Boulos et al., 1994; Yang et al., 2016). However, typical pyrometallurgical process gases may contain a variety of hydrogen, oxygen, carbon, and sulphur compounds combined with many metallic elements, and data for such complex mixtures are not readily available in open literature. This, combined with the difficulty of implementing first-principles plasma property calculations, has led to many previous authors, including those of this paper (Reynolds, 2018; Reynolds et al., 2010), to develop detailed arc models, which rely on highly oversimplified or approximated plasma property data from literature sources; the question arises of whether the results obtained in such work translate to the real industrial operations that such modelling is intended to represent. Recent work by (Makgoale et al., 2021) has comprehensively highlighted the sensitivity of arc models to approximations and simplifications, including material properties.

In this paper, a full methodology for calculating plasma properties from first principles for arbitrary mixtures is presented together with an open source software implementation developed for the Python programming language. The plasma property calculator is combined in a workflow together with traditional thermochemical process calculation tools, and applied to a number of Mintek DC arc furnace projects to demonstrate how process-specific plasma property data sets can be generated for use in further modelling.

Theory and methods – plasma calculations

Plasma property calculations are generally part of broader workflows, which connect metallurgical process information to practical aspects of DC furnace operation such as thermal performance and electrical behaviour. A typical example is shown in Figure 3.

The first step involves calculations using thermochemistry calculation tools such as FactSage (Bale et al., 2016) to obtain the composition of the gas phase in the furnace freeboard as a function of process parameters. This is followed by plasma property calculations as described in this paper to determine the behaviour of this gas at conditions inside the arc. Finally, this property information can be passed on to models of the arc to predict its behaviour for furnace design and operation purposes. In this paper the focus is primarily on the second step, for which the methods described here have been developed. The calculations are then demonstrated by application to a variety of DC arc furnace smelting processes.

Thermal plasmas of the sort found in the arcs of DC furnaces are often assumed to be in local thermodynamic equilibrium (LTE), meaning that the heavy particles such as ions and atoms are in thermal equilibrium with the much lighter electrons, and a single unique temperature can be assigned to all species (Boulos et al., 1994). A major advantage of the LTE approximation is that all thermophysical properties of a mixture of an arbitrary number of plasma species can be expressed as (complicated) functions of temperature, pressure, and initial composition only – the equilibrium composition is itself a function of these variables since it is uniquely determined by the state parameters and mass conservation, and the properties are in turn determined by the equilibrium composition.

Plasma composition

Given temperature, pressure, and a set of species present in a plasma (and some information about the elemental composition of the mixture if more than one element is present), the number density of each species at thermodynamic equilibrium can be calculated using the principle of Gibbs free energy minimisation (Boulos et

Figure 3—Modelling workflow for arc furnace applications

al., 1994). This is an important intermediate step in calculating the thermophysical properties and may also be useful in, its own right, if one is interested in the relative proportions of different species in complex plasmas. To start, recall the definition of Gibbs free energy:

$$G = G^0 + \sum_i \mu_i N_i \quad [1]$$

Where G is the Gibbs free energy of a system, G^0 is a reference value depending only on temperature and pressure, μ_i is the chemical potential of species i, and N_i is the absolute number of particles of species i present. In statistical mechanics, μ_i in J per particle is represented as:

$$\mu_i = E_i^0 - k_B T \ln\left(\frac{Q_{tot,i} V}{N_i}\right) \quad [2]$$

Where T is absolute temperature, k_B is the Boltzmann constant, Q is a statistical quantity called the partition function in m^{-3}, V is the volume of the system, and E_i^0 is a reference energy in J per particle of the species relative to its constituent uncharged atoms. For uncharged monatomic species and electrons $E_i^0 = 0$, for uncharged polyatomic species it is the negative of the dissociation energy, and for charged species it is E_i^0 of the species with one fewer charge number.

Consider, for example, a simple plasma system for hydrogen containing species H_2, H, H^+, and e^-. In this case $E_H^0 = E_e^0 = 0, E_{H_2}^0$ $D_{e,H_2\to 2H}$, and E_{H+}^0 = is $I_{e,H}$ where $D_{e,H_2\to 2H}$ is the dissociation energy of the diatomic hydrogen molecule, and $I_{e,H}$ is the ionisation energy of the hydrogen atom.

It is possible to substitute volume out of the equations by using the ideal gas law:

$$V = \frac{k_B T \sum_i N_i}{P} \quad [3]$$

Where P is the specified pressure of the system. A system at equilibrium is characterised by a minimum stationary point in G, giving an independent equation for each species i, which simplifies to:

$$\frac{\partial G}{\partial N_i} = \mu_i = 0 \quad [4]$$

This set of equations must be solved subject to constraints supplied by the conservation of mass of each element present:

$$\sum_i \nu_{ij} N_i = \eta_j^0 \quad [5]$$

Where ν_{ij} is the stoichiometric coefficient representing the number of atoms of element j present in species i, and η_j^0 is the (fixed) total number of atoms of element j present in the system, specified by the initial composition. Together with this, one additional constraint is supplied by the requirement for electroneutrality of the plasma:

$$\sum_i z_i N_i = 0 \quad [6]$$

Where z_i is the charge number of species i. The set of Equations in 4, 5, and 6 are solved using an iterative Lagrange multiplier approach to obtain the set of N_i, and hence number density $n_i = N_i/V$, at LTE starting from an initial guess.

Partition functions

The partition function for a particular species is a description of the statistical properties of a collection of atoms or molecules of that species at thermodynamic equilibrium. Partition functions are normally presented as the sum of weighted state probabilities across the possible energy states of the system. In general, at moderate plasma temperatures up to a few 10^4 K, a species' total partition function can be written as the product of several unique partition functions arising from different quantum mechanical phenomena (assuming weak state coupling and no contribution from nuclear states):

$$Q_{tot} = Q_t Q_{int} = Q_t Q_e Q_v Q_r \quad [7]$$

Here, Q_t is the translational partition function due to the species' ability to move around in space, Q_{int} is the internal partition function due to various energy states internal to the particles of the species, Q_e is the electronic partition function due to different possible arrangements of the electronic structure of the species, Q_v is the vibrational partition function due to the ability of the bonds in a polyatomic species to vibrate at different energy levels, and Q_r is the rotational partition function due to a species' ability to rotate around its center of mass at different energy levels.

Four different types of species are distinguished here: monatomic for charged or uncharged single atoms, diatomic for charged or uncharged bonded pairs of atoms, polyatomic for charged or uncharged bonded groups of three or more atoms, and free electrons. The formulae used for the various partition functions for each type are shown in Table 1 (Boulos et al., 1994; Herzberg, 1945; McQuarrie, 1973). Here m_i and m_e are the mass of one particle of the species concerned, $\hbar$ is the reduced Planck constant, g_j and E_j are the quantum degeneracy and energy (in J) of electronic energy level j with j=0 being the ground state, σ_s is the symmetry constant of a molecular species, and $\omega_{e,j}$, A_r, B_r, and C_r (all converted to J equivalent) are the vibrational, symmetry, and rotational constants, respectively, for a diatomic or polyatomic molecule.

In this study complete electronic energy level sets are implemented for single atoms and ions, but only the ground state level is considered for diatomic and polyatomic molecules. This is assumed to be a reasonable approximation, since these species are generally present only at low temperatures where electronic excitation is limited compared to vibrational and rotational states.

Ionisation energy lowering

The ionisation energy required to remove a single electron from a particle is a constant for that particular species when considered in isolation. However, in a mixture of different species and free electrons, the ionisation energy is lowered by a small amount due to local electrostatic shielding effects. This affects both the calculation of the partition functions (the summation of electronic state contributions for monatomic species ignores states with energies above the lowered ionisation energy) and the calculation of equilibrium plasma compositions (the equilibrium relationships are defined using the reference energy levels for each species, which in turn depend on the lowered ionisation energies). Ionisation energy lowering is a complex problem in plasma physics, but there exist many approximate methods for quantifying this effect using the theory of Debye-shielded potentials. Provided the same method is used for all species, the calculation errors generally remain small (Boulos et al., 1994).

In the present work an approximate analytical solution is used (Stewart, Pyatt, 1966). In this method, the ionisation energy lowering for each charged species is calculated explicitly using:

$$\frac{\delta I_{e,i}}{k_B T} = \frac{\left(\left(\frac{a_i}{l_D}\right)^3 + 1\right)^{\frac{2}{3}} - 1}{2(z^* + 1)}$$
$$z^* = \frac{\sum_j z_j^2 n_j}{\sum_j z_j n_j}, \quad a_i = \left(\frac{3 z_i}{4\pi n_e}\right)^{\frac{1}{3}}, \quad [8]$$
$$l_D = \left(\frac{\epsilon_0 k_B T}{4\pi e^2 (z^* + 1) n_e}\right)^{\frac{1}{2}}$$

Table 1
Partition function expressions

Partition function	Monatomics	Diatomics	Polyatomics	Electrons
Q_t, 1/m³	$\left(\frac{m_i k_B T}{2\pi\hbar^2}\right)^{\frac{3}{2}}$	$\left(\frac{m_i k_B T}{2\pi\hbar^2}\right)^{\frac{3}{2}}$	$\left(\frac{m_i k_B T}{2\pi\hbar^2}\right)^{\frac{3}{2}}$	$\left(\frac{m_i k_B T}{2\pi\hbar^2}\right)^{\frac{3}{2}}$
Q_e, dim'less	$\sum_j g_j \exp\left(-\frac{E_j}{k_B T}\right)$	g_0	g_0	2
Q_v, dim'less	1	$\frac{\exp\left(-\frac{\omega_e}{k_B T}\right)}{1-\exp\left(-\frac{\omega_e}{k_B T}\right)}$	$\prod_j \frac{\exp\left(-\frac{\omega_{e,j}}{k_B T}\right)}{1-\exp\left(-\frac{\omega_{e,j}}{k_B T}\right)}$	1
Q_r, dim'less	1	$\frac{k_B T}{\sigma_s B_r}$	$\frac{k_B T}{\sigma_s B_r}$ or $\frac{1}{\sigma_s}\left(\frac{\pi k_B T}{A_r B_r C_r}\right)^{\frac{1}{2}}$	1

Here, $\delta I_{e,i}$ is the ionisation energy lowering of species i (in J), a_i is the ion-sphere radius of species i, l_D is the Debye sphere radius, z^* is the effective charge number in a plasma consisting of a mixture of species of different charges, z_j is the charge number of species j, n_j is the number density (particles per cubic meter) of species j, and e is the elementary charge.

It should be noted that the method of Griem has been used extensively for previous work in the field (Griem, 1964), and slight differences may exist compared to the method of Steward and Pyatt used here.

Thermodynamic properties

Given a plasma composition in terms of number densities n_i, the mass density ρ, the enthalpy H, and the heat capacity C_P can be calculated directly.

Plasma density

The plasma mass density is a straightforward calculation:

$$\rho = \frac{1}{N_A}\sum_i n_i M_i \qquad [9]$$

Where M_i is the molar mass of species i in kg/mol, and N_A is Avogadro's constant.

Plasma enthalpy

Calculation of the plasma enthalpy at a particular temperature, pressure, and species composition is performed using the statistical mechanics definition of internal energy:

$$U = -\sum_j \frac{1}{Q_j}\frac{\partial Q_j}{\partial \beta} \qquad [10]$$

Where U is the internal energy in J for a single particle of a particular species, Q_j are the various kinds of partition functions making up Q_{tot} for the species, and $\beta = 1/k_B T$. Formulae for U of various plasma species are thus readily produced using the partition function expressions given earlier. Once the internal energy is known, enthalpy can be calculated from its definition:

$$H = U + pV \qquad [11]$$

When multiple species are present, the relative reference energy E_i^0 for each species must also be included. Application of the ideal gas law to the pV term then gives:

$$H_i = U_i + E_i^0 + k_B T \qquad [12]$$

Where H_i is the enthalpy of species i in J per particle. Summing over all component species of a plasma and dividing by the density then gives the specific enthalpy of the mixture in J/kg:

$$H = \frac{\sum_i n_i H_i}{\rho} = N_A \frac{\sum_i n_i H_i}{\sum_i n_i M_i} \qquad [13]$$

It is important to note that the values obtained may be relative to an arbitrary non-zero value in general, and caution should be exercised when comparing enthalpy calculations for different mixtures.

Heat capacity

Direct calculation of C_P given an arbitrary plasma composition is possible if some knowledge of the reaction paths between species is also supplied. Although any set of consistent reaction paths will give the same result at equilibrium, choosing one actual set of paths from the many possible options implies that it represents reality, and this is certainly open to some debate. It is therefore simpler to avoid the need for any such choices by calculating heat capacity using a numerical derivative of the mixture enthalpy around the temperature of interest:

$$C_P = \left(\frac{\partial H}{\partial T}\right)_P \approx \frac{H(T+\Delta T, P) - H(T-\Delta T, P)}{2\Delta T} \qquad [14]$$

Transport properties

Transport properties of plasmas are calculated using Chapman-Enskog theory developed from the principles of statistical mechanics. This is well described in (Chapman, Cowling, 1990; Devoto, 1966).

Collision integrals

For the calculation of transport properties of a mixture of particles in a dilute phase such as gas or plasma as a function of temperature and pressure, information is needed about both the composition of the mixture in terms of the species present, and the nature of collisions between pairs of particles. The former is obtained from free energy minimisation procedures described in the aforementioned, and the latter is described using quantities called collision integrals. Collision integrals are calculated as the effective geometric cross section between a given pair of particles, which is in general dependent on the physical nature of each particle as well as their closing velocity.

The collision integral in terms of integer moments l and s is derived from the gas-kinetic cross section σ_{ij} (χ,g) by two successive integrations as follows (Chapman, Cowling, 1990):

$$\Omega_{ij}^{(l)} = 2\,\pi \int_0^{\pi} \sigma_{ij}(\chi, g)\left(1 - \cos^{l}\chi\right)\sin\chi d\chi \qquad [15]$$

$$\bar{\Omega}_{ij}^{(l,s)} = \frac{4(l+1)}{(s+1)!\,(2l+1-(-1)^{l})}\int_0^{\infty} e^{-\gamma^2}\gamma^{2s+3}\Omega_{ij}^{(l)}(g)d\gamma \qquad [16]$$

Where χ is the collision deflection angle, g is the closing velocity, and:

$$\gamma^2 = \frac{m_r g^2}{2k_B T}, \quad m_r = \frac{m_i m_j}{m_i + m_j} \qquad [17]$$

Where m_r is the reduced mass of the colliding pair, and m_i are the particle masses. In general, collision integrals depend in complex ways on the interaction potential between the colliding pair, which may have both classical and quantum mechanical components. As they are often difficult to calculate efficiently in closed forms, this has led to the development of many approximate or empirical expressions for various types of collisions. In the present work we distinguish different collision-pair types as shown in Table 2.

Elastic collision integrals $\Theta_{nn/in}$ for collisions between neutral heavy species or neutrals and ions are calculated using the empirical formulae of Laricchiuta et al. (2007). These were obtained by fitting to classical trajectory models using an extended and generalised Lennard-Jones type potential. The Laricchiuta expressions have the advantage of depending on only a few fundamental properties of the colliding species: their polarisability, the effective number of electrons contributing to polarisation, and the charge number in the case of neutral-ion collisions.

$$\begin{aligned}\ln\left(\frac{\Theta_{nn/in}}{\pi r_{LJ}^2}\right) &= \frac{A_1 + A_2\ln\left(\frac{k_B T}{\epsilon_{LJ}}\right)}{1+\exp(-2\xi_1)} + \frac{A_5}{1+\exp(-2\xi_2)} \\ \xi_1 &= \frac{\ln\left(\frac{k_B T}{\epsilon_{LJ}}\right) - A_3}{A_4}, \quad \xi_2 = \frac{\ln\left(\frac{k_B T}{\epsilon_{LJ}}\right) - A_6}{A_7}\end{aligned} \qquad [18]$$

In these expressions r_{LJ} and ϵ_{LJ} are parameters related to the Lennard-Jones potential used and are defined in terms of the colliding species' polarisabilities, effective electrons, and charge if applicable. A_i are polynomials in a parameter called 'softness', which is determined from the species' polarisabilities. A full description of the model including tabulations of the polynomial coefficients for (l,s) in the range 1 to 4 is available in (Laricchiuta et al., 2007).

The inelastic resonant charge transfer integral Θ_{tr} is only used for collisions between first ions and neutrals of the same species. It is obtained from approximate quantum mechanical calculations of an electron moving in the potential between two identical nuclei (Devoto, 1967; Rapp, Francis, 1962; Smirnov, 1971):

$$\begin{aligned}\Theta_{tr} = {} & B_1^2 - B_1 B_2 \bar{R} + \left(\frac{B_2\bar{R}}{2}\right)^2 \\ & + \frac{B_2\zeta_1}{2}(B_2\bar{R} - 2B_1) + \frac{B_2^2}{4}\left(\frac{\pi^2}{6} - \zeta_2 + \zeta_1^2\right) \\ & + \frac{B_2}{2}(B_2(\bar{R}+\zeta_1) - 2B_1)\ln\frac{T}{M} + \left(\frac{B_2}{2}\ln\frac{T}{M}\right)^2 \\ B_1 = {} & \pi\frac{9.817\times10^{-9}}{I_e^{0.729}}, \quad B_2 = \pi\frac{4.783\times10^{-10}}{I_e^{0.657}} \\ \bar{R} = {} & \ln 4R, \quad \zeta_1 = \sum_{n=1}^{s+1}\frac{1}{n}, \quad \zeta_2 = \sum_{n=1}^{s+1}\frac{1}{n^2},\end{aligned} \qquad [19]$$

Table 2

Collision integrals for interaction between different particles

	Neutral	Ion	Electron
Neutral	$\bar{\Omega}_{ij}^{(l,s)} = \Theta_{nn/in}$	$\bar{\Omega}_{ij}^{(l,s)} = \Theta_{nn/in}, \Theta_{tr}$	$\bar{\Omega}_{ij}^{(l,s)} = \Theta_e$
Ion	$\bar{\Omega}_{ij}^{(l,s)} = \Theta_{nn/in}, \Theta_{tr}$	$\bar{\Omega}_{ij}^{(l,s)} = \Theta_c$	$\bar{\Omega}_{ij}^{(l,s)} = \Theta_c$
Electron	$\bar{\Omega}_{ij}^{(l,s)} = \Theta_e$	$\bar{\Omega}_{ij}^{(l,s)} = \Theta_c$	$\bar{\Omega}_{ij}^{(l,s)} = \Theta_c$

R is the universal gas constant, M is the molar mass of the species, and I_e is its first ionisation energy in eV.

For collisions between charged particles, the collision integral Θ_c is calculated from classical trajectories of charges moving in a Coulombic potential. This is found to depend on a quantity called the Coulomb logarithm, ln Λ Approximate empirical expressions are available for ln Λfor three important classes of collisions: electron-electron, electron-ion, and ion-ion. For the temperature ranges of interest in thermal plasma calculations, and assuming LTE conditions, these are (Richardson, 2019:

$$\ln\Lambda_{e-e} = 23.5 - \ln\left(n_e^{\frac{1}{2}}T^{-\frac{5}{4}}\right) - \left(10^{-5} + \frac{(\ln T - 2)^2}{16}\right)^{\frac{1}{2}} \qquad [20]$$

$$\ln\Lambda_{e-ion} = 23 - \ln\left(n_e^{\frac{1}{2}}z_i T^{-\frac{3}{2}}\right) \qquad [21]$$

$$\ln\Lambda_{ion-ion} = 23 - \ln\left[\frac{z_i z_j}{T}\left(\frac{n_i z_i^2 + n_j z_j^2}{T}\right)^{\frac{1}{2}}\right] \qquad [22]$$

The appropriate expression for l Λ is then used to calculate the overall collision integral for charged particles (Devoto, 1967), where γ is the Euler gamma constant:

$$\begin{aligned}\Theta_c &= \frac{\pi C_1}{s(s+1)}\left(\frac{z_i z_j e^2}{2k_B T}\right)^2\left(\ln\Lambda - C_2 - 2\bar{\gamma} + \sum_{n=1}^{s-1}\frac{1}{n}\right) \\ C_1^{l=1} &= 4, C_1^{l=2} = 12, C_1^{l=3} = 12, C_1^{l=4} = 16 \\ C_2^{l=1} &= \frac{1}{2}, C_2^{l=2} = 1, C_2^{l=3} = \frac{7}{6}, C_2^{l=4} = \frac{4}{3}\end{aligned} \qquad [23]$$

Calculation of the electron-neutral collision integral Θ_e from first principles is an extremely complex process and requires detailed knowledge of quantum mechanical properties of the target species. The complexity also increases rapidly as the atomic mass of the target increases and multiple excited states become relevant. For the present work a simple empirical formulation was developed instead, which can be fitted to experimental or theoretical data to obtain an estimate of the collision integral for the neutral species of interest:

$$\Omega_{ej}^{(l)} \approx D_1 + D_2\left(\frac{m_r g}{\hbar}\right)^{D_3}\exp\left(-D_4\left(\frac{m_r g}{\hbar}\right)^2\right) \qquad [24]$$

In cases where insufficient data is available, a very crude hard sphere cross section approximation can be made by specifying only D_1 and setting the remaining D_i to zero. In all other cases, the D_i are fitted to momentum cross section curves obtained from literature sources. Performing the second collision integral integration step from Equation 16 then yields:

$$\begin{aligned}\Theta_e &= D_1 + \frac{\Gamma\left(s+2+\frac{D_3}{2}\right)D_2\tau^{D_3}}{\Gamma(s+2)(D_4\tau^2+1)^{s+2+\frac{D_3}{2}}}, \\ \tau &= \frac{(2m_r k_B T)^{\frac{1}{2}}}{\hbar}\end{aligned} \qquad [25]$$

In the Chapman-Enskog formulation, the solutions to the Boltzmann transport equation are found to depend on quantities called bracket integrals. The bracket integrals are expanded using associated Laguerre polynomials, approximated to a specified number of terms indicated by integers m and p (Chapman, Cowling, 1990). This produces expressions, which are functions of the particle masses, concentrations, and collision integrals. These expressions are then combined in a matrix representing the set of binary collisions between all species in the plasma at a given level of approximation. For example, the matrix entries for the lowest approximation level are given by:

$$q_{ij}^{m=0,p=0} = 8\sum_{l}\frac{n_l m_l^{\frac{1}{2}}}{(m_i+m_l)^{\frac{1}{2}}}\bar{\Omega}_{il}^{(1,1)} \left[n_i\left(\frac{m_i}{m_j}\right)^{\frac{1}{2}}(\delta_{ij}-\delta_{jl}) - n_j\frac{(m_i m_j)^{\frac{1}{2}}}{m_i}(1-\delta_{il})\right] \quad [26]$$

Where δ_{ij} is the Kronecker delta. Full q matrix entry expressions for m and p from 0 to 3 are available in the appendices of Devoto (1966). Different expressions are used depending on whether the property being calculated is related to mass or momentum transport – in the present work Devoto's convention is adopted and they are indicated as q_{ij}^{mp} and q_{ij}^{mp}, respectively.

Mass and thermal diffusion coefficients

Although not generally of direct interest in equilibrium calculations where diffusion kinetics do not play a role, the binary and thermal diffusion coefficients are an important intermediate calculation step for other properties of interest. As per Devoto (1966) we have:

$$\mathcal{D}_{ij} = \frac{\rho n_i}{2nm_j}\left(\frac{2\,k_B T}{m_i}\right)^{\frac{1}{2}} c_{i0}^{ji} \quad [27]$$

$$\mathcal{D}_i^T = \frac{n_i m_i}{2}\left(\frac{2\,k_B T}{m_i}\right)^{\frac{1}{2}} a_{i0} \quad [28]$$

Where the a and c values are calculated by solution of the linear systems:

$$\sum_j\sum_{p=0}^{\mathcal{M}} q_{ij}^{mp} c_{jp}^{hk} = 3\pi^{\frac{1}{2}}(\delta_{ik}-\delta_{ih})\delta_{m0} \quad [29]$$

$$\sum_j\sum_{p=0}^{\mathcal{M}} q_{ij}^{mp} a_{jp} = -\frac{15\pi^{\frac{1}{2}} n_i}{2}\delta_{m1} \quad [30]$$

The indices i, j, h, and k range over the number of species present in the plasma and indices m and p range from 0 to M, the maximum q-matrix approximation level.

Plasma viscosity

As per Devoto (1966), viscosity μ of a plasma mixture is given by:

$$\mu = \frac{k_B T}{2}\sum_j n_j b_{j0} \quad [31]$$

Where values for b are obtained from the solution of the linear system:

$$\sum_j\sum_{p=0}^{\mathcal{M}} \hat{q}_{ij}^{mp} b_{jp} = 5n_i\left(\frac{2\pi m_i}{k_B T}\right)^{\frac{1}{2}}\delta_{m0} \quad [32]$$

Plasma electrical conductivity

Although conduction by ions does contribute to the overall electrical conductivity σ of a plasma mixture, the effect is generally very small due to the large mass difference between electrons and ionic species and can be neglected. Using this approximation, we have per Devoto (1966):

$$\sigma \approx \frac{e^2 n}{\rho k_B T}\sum_{j\neq e} n_j m_j z_j \mathcal{D}_{ej} \quad [33]$$

Where n is the total number density of the plasma in particles per m^3, and D_{ej} are the binary diffusion coefficients of electrons relative to the heavy species.

Plasma thermal conductivity

The effective heat flux in equilibrium plasmas is a combination of several terms describing molecular transport, thermal diffusion, and chemical reaction. These can be rearranged in a variety of ways depending on the application, but one of the forms given in Devoto (1966) is particularly useful:

$$\mathbf{q} = \sum_j\left(\frac{n^2 m_j}{\rho}\sum_i m_i H_i \mathcal{D}_{ij} - \frac{n k_B T \mathcal{D}_i^T}{n_j m_j}\right)\mathbf{d_j} - \left(\kappa' + \sum_j\frac{H_j \mathcal{D}_j^T}{T}\right)\nabla T \quad [34]$$

If we consider an equilibrium system at constant pressure and with no external forces, we have:

$$\mathbf{d_j} = \nabla x_j = \frac{dx_j}{dT}\nabla T \quad [35]$$

Where x_j are the mole fractions of the species present in the plasma. By substituting Equation 35 into 34, the total thermal conductivity κ can be expressed as the pre-multiplication factor to ∇T in the heat flux expression:

$$\kappa = -\sum_j\left(\frac{n^2 m_j}{\rho}\sum_i m_i H_i \mathcal{D}_{ij} - \frac{n k_B T \mathcal{D}_i^T}{n_j m_j}\right)\frac{dx_j}{dT} + \kappa' + \sum_j\frac{H_j \mathcal{D}_j^T}{T} \quad [36]$$

The molecular thermal conductivity κ' is determined using the a values obtained from Equation 30:

$$\kappa' = \frac{5k_B}{4}\sum_j n_j\left(\frac{2\,k_B T}{m_j}\right)^{\frac{1}{2}} a_{j1} \quad [37]$$

As in the case of the plasma heat capacity it is possible to develop analytical expressions for the $\frac{dx_j}{dT}$ term if some assumptions are made about reaction pathways, but as before this can be avoided simply by evaluating the derivative numerically at the temperature of interest:

$$\frac{dx_j}{dT} \approx \frac{x_j(T+\Delta T, P) - x_j(T-\Delta T, P)}{2\Delta T} \quad [38]$$

Radiation properties

Thermal radiation in plasmas is an extensive topic of study on its own and covers a broad range of phenomena including line emission and absorption, continuum radiation, quantum mechanical effects, and many others. These are well documented in references such as (Boulos et al., 1994). Calculation of radiation behaviour becomes highly complex when absorption effects are considered – in the present work these effects are not explored, and only an estimate of the total emission coefficient is calculated. It should be noted that particularly in the case of metallic atoms and ions, line broadening and the associated absorption effects can be very strong indeed and the results here should therefore be taken as indicative of relative behaviour only.

For certain analyses, radiation emission can be combined with thermal conductivity to produce a lumped effective thermal conductivity κ_{eff}. This is a useful approximation for simple analytical calculations in optically thick plasmas where reabsorption of emitted radiation is high, and a rigorous treatment of the radiation transport is not practical. In such cases, κ_{eff} values including radiation diffusion terms can be orders of magnitude higher than the true thermal conductivity (Howell et al., 2020).

Total radiation emission coefficient

To a good first approximation in the temperature ranges of interest to thermal plasma applications, the total emission from a plasma mixture can be assumed to be purely line radiation from transitions between excited states in the constituent species. This can be calculated simply by integrating over wavelengths between 0 and ∞ for each line in the emission spectrum for each species and summing the results. As per Boulos et al. (1994), the formula for atomic species is:

$$\epsilon_{tot} \approx \frac{\hbar c}{2} \sum_j \sum_{\mathcal{L}} \frac{n_j g_{j,\mathcal{L}} \mathcal{A}^j_{\mathcal{L}}}{Q^j_e \lambda_{j,\mathcal{L}}} \exp\left(-\frac{E_{j,\mathcal{L}}}{k_B T}\right) \quad [39]$$

Line wavelengths $\lambda_{j,L}$, state degeneracies $g_{j,L}$, transition probabilities $\mathcal{A}^j_{\mathcal{L}}$, and energy levels $E_{j,\mathcal{L}}$ are readily available for most elements in atomic spectroscopy databases.

Similar expressions can be developed for molecular species, but these are neglected here as they are only present at very low plasma temperatures where the total emission is relatively small, and some inaccuracy can be tolerated. The emission spectrum for molecules is also predominantly from rotational and vibrational modes, and these generally have much smaller $\mathcal{A}^j_{\mathcal{L}}$ values than those of the electronic emission lines of atoms and ions.

Software implementation

The plasma properties calculations described in the aforementioned have been implemented in an open source software package for the Python programming language, 'minplascalc'. The package uses a flexible object-oriented representation of plasma species and mixtures to perform a range of LTE calculations on arbitrary mixtures, assuming data for the constituents are available. Direct calculation of plasma properties is implemented using high-level functions, improving repeatability and providing a simple and straightforward user experience. The code is under active development, and along with documentation and usage instructions, is available online (Reynolds, Sandrock, 2024).

Results and discussion

In this section we present new results from thermochemical modelling and plasma property calculations for a range of DC arc furnace smelting processes, all of which were tested to large pilot plant scale at Mintek during the period from 1970 to 2020.

In each case the procedure was to first calculate the equilibrium gas composition over the process using FactSage software, and then pass the elemental gas composition into the minplascalc software to calculate the thermophysical properties of the plasma at arc temperatures. The FactSage calculations are performed at a range of different slag temperatures between the typical operating temperature for the process and the effective vaporisation temperature (the lowest temperature at which all process material is in the gas phase). This reflects the possibility of very large temperature gradients in the slag bath in the vicinity of the arc attachment zone in DC furnaces (Barcza et al., 1990).

Thermochemical simulations were done using FactSage 8.3. In all simulations, the FactPS database was used to represent selected pure solid species, while the gas phase was modelled with the gaseous ions option enabled. For the slag phase in all simulations, the FTOxid database was used. For the ferrochromium, ilmenite, and ferronickel processes the SGTE alloy solution database was employed, while for the Conroast, Enviroplas, and Mintek Thermal Magnesium processes, the metallic and/or matte solutions were approximated using the FTmisc database.

Species data for plasma property calculations in minplascalc was obtained from various sources as listed in Table 3 and Table 4:

(a) NIST Atomic Spectra Database (Kramida and Ralchenko, 1999).
(b) NIST CCCBDB (Johnson, 2022).
(c) New ab initio calculations conducted for the present work (see further description in the following).
(d) LXCat (Carbone et al., 2021).
(e) Estimated using empirical polarisation potentials (Laricchiuta et al., 2007).

Additional information was also sourced from NIST Chemistry Webbook (Linstrom, 1997).

Data flagged as (c) were obtained from computations using density functional theory employing the PBE0 hybrid exchange functional (Adamo, Barone, 1999) and the aug-cc-pVTZ basis sets (Balabanov, Peterson, 2005; Hill, Peterson, 2017; Kendall et al., 1992; Prascher et al., 2011; Woon, Dunning, 1993). Pseudopotentials comprising aug-cc-pVTZ-PP basis functions (Peterson, 2003) for valence electrons and the associated relativistic small-core Stuttgart/Cologne pseudopotential functions (Metz et al., 2000) were used to describe the elements Sn and Pb. Basis sets and pseudopotentials not available by default in the software were obtained from online databases (Feller, 1996; Pritchard et al., 2019; Schuchardt et al., 2007). All computations were performed using Gaussian 16 (Frisch et al., 2016).

Static polarisabilities were calculated analytically using the Kohn-Sham equivalent of the Coupled Perturbed Hartee-Fock equations. Adiabatic ionisation energies I_e were calculated at 0 K from electronic energies of the neutral ($E_{neutral}$) and cationic (E_{cation}) form of each plasma species, corrected for zero-point energy (ZPE), as $Ie = E_{cation} - E_{neutral}$.

Dissociation energies at 0 K were likewise calculated from the difference in the ZPE-corrected energies of the constituent atoms and the parent molecule, each in their lowest energy spin states.

Table 3

Data sources for monatomic species

Species	Energy levels	Emission lines	Polarisability	Ionisation energy	Electron cross section
Ar, Ar^{z+}	(a)	(a)	(b)	(a)	(d)
C, C^{z+}, Cu, Cu^{z+}, H, H+, Mg, Mg^{z+}, O, O^{z+}	(a)	(a)	(c)	(a)	(d)
Al, Al^{z+}; Ca, Ca^{z+}; Co, Co^{z+}; Cr, Cr^{z+}; Fe, Fe^{z+}; Mn, Mn^{z+}; Ni, Ni^{z+}; Pb, Pb^{z+}; S, S^{z+}; Si, Si^{z+}; Ti, Ti^{z+}; Zn, Zn^{z+}	(a)	(a)	(c)	(a)	(e)

Table 4

Data sources for diatomic and polyatomic species

Species	Vibration and rotation constants	Polarisability	Electron cross section
CO, CO_2, H_2O, O_2, SO_2	(c)	(c)	(d)
AlO, CaO, CrO, FeO, MgO, NiO, OH, PbO, SO, SiO, TiO	(c)	(c)	(e)
H_2	(b)	(b)	(d)
SiS	(b)	(b)	(e)

ZPE and fundamental vibrational frequencies were scaled by a factor of 0.962 to correct for anharmonicity and deficiencies in the level of theory (Johnson, 2022).

DC ferrochromium process

DC arc furnace smelting technology for the production of ferrochromium has been in industrial use for over forty years, with its first implementation dating back to 1984 (Barcza, 1986). This technology evolved to address the 'fines problem' encountered by South African ferrochrome producers, where the availability of traditional lumpy ore was diminishing, and the friable nature of the remaining ores led to the generation of high proportions of fines. DC smelting offered an efficient solution by processing these fine materials without the need for agglomeration. The process can be optimised for high efficiencies due to the high-intensity arc attachment zone in the open-arc furnace. Ferrochrome production occurs at very high temperatures, where chromite ore, along with fluxes such as lime and silica, reacts with a carbonaceous reducing agent. Slag modifiers are used to adjust the liquidus temperature and viscosity of the slag, ensuring optimal metal recovery. In a DC operation, maintaining a continuous balance of power and feed is crucial, with the arc attachment zone acting as the engine room where these elements are harmonised to meet the smelting objectives. The bulk chemistry of the slag and metal bath in the DC smelter is fairly uniform, enabling high metal conversion, while the configuration minimises metal entrainment in the slag, resulting in high metal recoveries. Because the power input in a DC arc smelting furnace is relatively independent of slag properties, it is possible to adjust the slag composition to optimally recover metal and produce a desired product, such as one with lower or higher silicon content. Over the years DC smelting for ferrochrome production has matured, with power ratings of installations increasing from 12 MW to 72 MW.

Thermochemical simulations in FactSage were based on the composition of South African MG ore (42.9% Cr_2O_3), for which the full composition can be found in (Geldenhuys, 2013). Anthracite with a dry fixed carbon content of 83.5%, 6.5% volatiles, 10% ash, and 2% moisture was assumed to be the reductant for the process; the detailed composition of the reductant ash can be found in the patent of Denton and Schoukens (1993). For these simulations the small amounts of Na, K, P, and V oxides in the ore and reductants were ignored. For 100 kg of ore, it was assumed that 13 kg of CaO, 8.6 kg of SiO_2, and 22 kg of anthracite reacts in the DC furnace at slag temperatures between 2023 K and the vaporisation temperature of 3590 K, with a simulated step size of 25 K. The choice of fluxing was guided by slag composition targets from Geldenhuys (2013). Volatiles were approximated as CH_4. In FactSage, the option to calculate all transitions was also enabled; this aids in finding appropriate points where phase transitions such as boiling take place.

For calculation of the plasma properties the minplascalc species set included Al, C, Ca, Cr, Fe, H, Mg, O, Si, Ti, Al^+, C^+, Ca^+, Cr^+, Fe^+, H^+, Mg^+, O^+, Si^+, Ti^+, Al^{2+}, C^{2+}, Ca^{2+}, Cr^{2+}, Fe^{2+}, Mg^{2+}, O^{2+}, Si^{2+}, Ti^{2+}, Al^{3+}, C^{3+}, Ca^{3+}, Cr^{3+}, Fe^{3+}, Mg^{3+}, O^{3+}, Si^{3+}, Ti^{3+}, SiO, FeO, MgO, CaO, CrO, AlO, CO_2, H_2O, CO, O_2, OH, and H_2. For a selection of slag temperatures over the range shown in Figure 4, the calculations were run between 2000 K and 30000 K at a pressure of one atmosphere. The results are given in Figure 5, with properties of pure CO plasma as a reference.

In ferrochromium smelting there is a clear distinction in plasma properties generated by gas formed by slag at temperatures $T_s > 2400$ K, and those for $T_s < 2400$ K. This is because very few of the metallic species apart from magnesium evaporate below this temperature, and the plasma gas is mainly carbon monoxide with some hydrogen from moisture and volatiles in the feed. The properties in this range are quite close to those of pure CO, with the exception of the radiation emission coefficient and electrical conductivity – these both show significant deviations at plasma temperatures of 3000 K to 7000 K, which are important for arc behaviour. This is likely due to the presence of trace amounts of magnesium in the gas phase even at relatively low process slag temperatures.

DC ilmenite process

Ilmenite is smelted to produce TiO_2-containing titania slag, primarily for pigment production (Pistorius, 2008). In South Africa, ilmenite from beach sands is a prime example of deposits not amenable to direct processing due to their high iron content. The smelting process acts as a concentration step at high temperatures

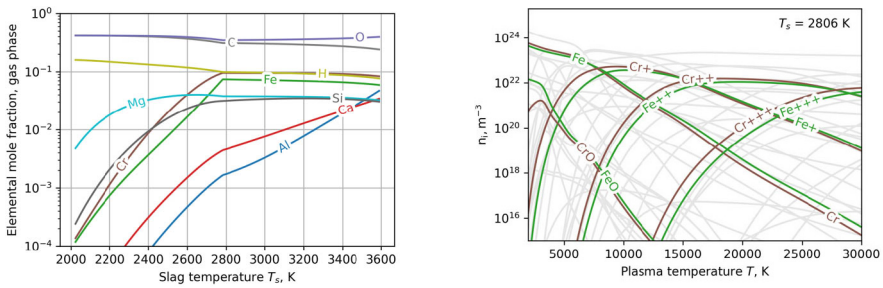

Figure 4—(*l*) Thermochemical calculation of elemental composition of the gas phase during DC ferrochromium smelting, (*r*) example plasma species composition calculation at T_s = 2806 *K* with Fe and Cr species highlighted

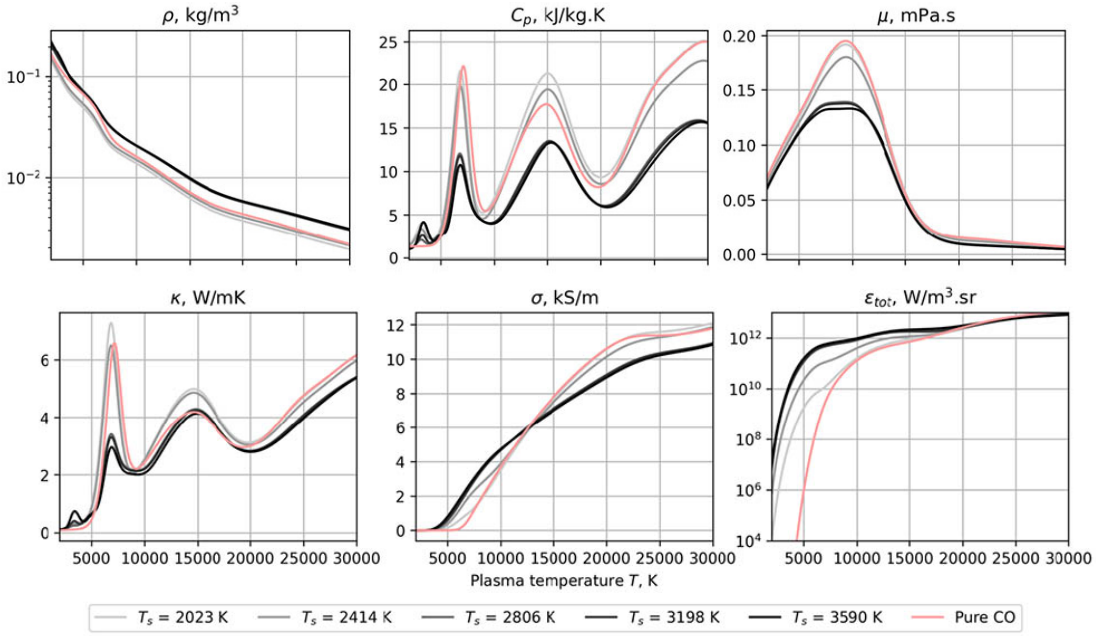

Figure 5—Thermophysical properties of plasmas generated from process gas in DC ferrochromium smelting

whereby iron is rejected through carbothermic reduction, yielding an economically valuable by-product, while the stable titania oxide is concentrated in the slag. Initially developed from ironmaking processes, the smelting of titaniferous feedstocks saw significant advancement in the 1950s with the commissioning of large electric furnaces at Sorel in Canada, designed to smelt low-grade titaniferous deposits in Quebec into titania-rich slag. The high electrical conductivity of titania slags and the need for precise slag composition control make conventional submerged-arc technology unsuitable, as carbon-based electrodes would come into direct contact with the melt. This high conductivity also limits heat generation through resistance, leading to the adoption of open-arc mode for large-scale smelting of titania-rich slags. The Sorel process was replicated in South Africa at Richards Bay Minerals in the mid-1970s for processing beach sand concentrate in six-in-line rectangular AC furnaces.

The application of DC smelting for ilmenite emerged in the mid-1990s as an alternative to the Sorel and Richards Bay furnace technologies. Led by Mintek and the Anglo American Corporation, DC technology was first implemented at Namakwa Sands on the West Coast of South Africa. These DC smelters, despite their smaller furnace capacities compared to the larger six-in-line furnaces, are economically viable and offer a flexible alternative to mega-scale furnace technology, enabling new producers to enter the slag market and providing operations with the flexibility that multiple smaller units offer. The metallurgical process is technologically agnostic, but with a single electrode and DC power, the control of the open-arc operation is arguably simpler in the DC units compared to the larger six-in-line furnaces. Unlike ferrochrome production, the selection of DC technology for ilmenite smelting is not driven by substantial process benefits, but the DC furnace offers a smaller footprint and greater operational flexibility. This has made it an attractive alternative, especially in South Africa, where four such furnaces operate with power ratings ranging from about 25 MW to 35 MW (Geldenhuys et al., 2021).

For FactSage simulation of the ilmenite process the composition of the ore and anthracite as per the patent of Denton and Schoukens (1993) was used, excluding the small amounts of V, Na, K, and P oxides that were used as inputs to the simulation. Test series C in the patent was chosen as an example case, normalised to 100 kg of ore and 13.9 kg anthracite. This process is considered fluxless. Simulations were done from 1873 K to the vaporisation temperature of 3659 K in this case, with the same step size as for other simulations.

For calculation of the plasma properties the minplascalc species set included Al, C, Ca, Cr, Fe, H, Mg, Mn, O, Si, Ti, Al^{+}, C^{+}, Ca^{+}, Cr^{+}, Fe^{+}, H^{+}, Mg^{+}, Mn^{+}, O+, Si^{+}, Ti^{+}, Al^{2+}, C^{2+}, Ca^{2+}, Cr^{2+}, Fe^{2+}, Mg^{2+}, Mn^{2+}, O^{2+}, Si^{2+}, Ti^{2+}, Al^{3+}, C^{3+}, Ca^{3+}, Cr^{3+}, Fe^{3+}, Mg^{3+}, Mn^{3+}, O^{3+}, Si^{3+}, Ti^{3+}, SiO, FeO, AlO, TiO, CO_2, H_2O, CO, O_2, OH, and H_2. For a selection of slag temperatures over the range shown in Figure 6, the calculations were run between 2000 K and 30000 K at a pressure of one atmosphere. The results are given in Figure 7, with properties of pure CO plasma as a reference.

In ilmenite smelting the process gas composition at low slag temperatures is again close to pure carbon monoxide, with some added hydrogen from contaminants in the feed material. The plasma properties are very similar to those of pure CO up to $T_s \approx$ 2300 K, after which they deviate significantly as metallic species begin to evaporate in significant quantities. It is interesting to note the appearance of multiple peaks in the plasma C_P and κ curves as T_s increases – this is likely due to the introduction of Ti species into the gas at high slag temperatures.

DC ferronickel process

Laterites and other oxidised nickel ores constitute a significant portion of global nickel reserves and typically require calcining prior to smelting, which generates calcine consisting of fine particles as the ores decompose during calcining. Smelting nickel laterite ores to produce ferronickel involves a trade-off between recovery and grade. A carbonaceous reductant is added to calcined laterite ore to reduce both iron and nickel. By selectively reducing iron, the slag and alloy composition can be adjusted to optimise nickel recovery while minimising excessive iron reduction. Increased reduction enhances nickel recovery but can dilute the nickel grade with iron.

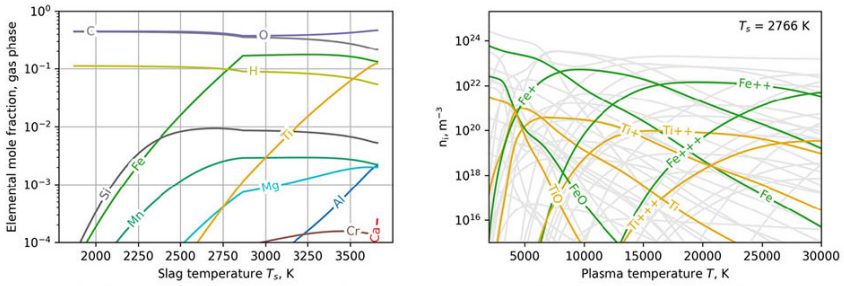

Figure 6—(*l*) Thermochemical calculation of elemental composition of the gas phase during DC ilmenite smelting, (*r*) example plasma species composition calculation at T_s = 2766 *K* with Fe and Ti species highlighted

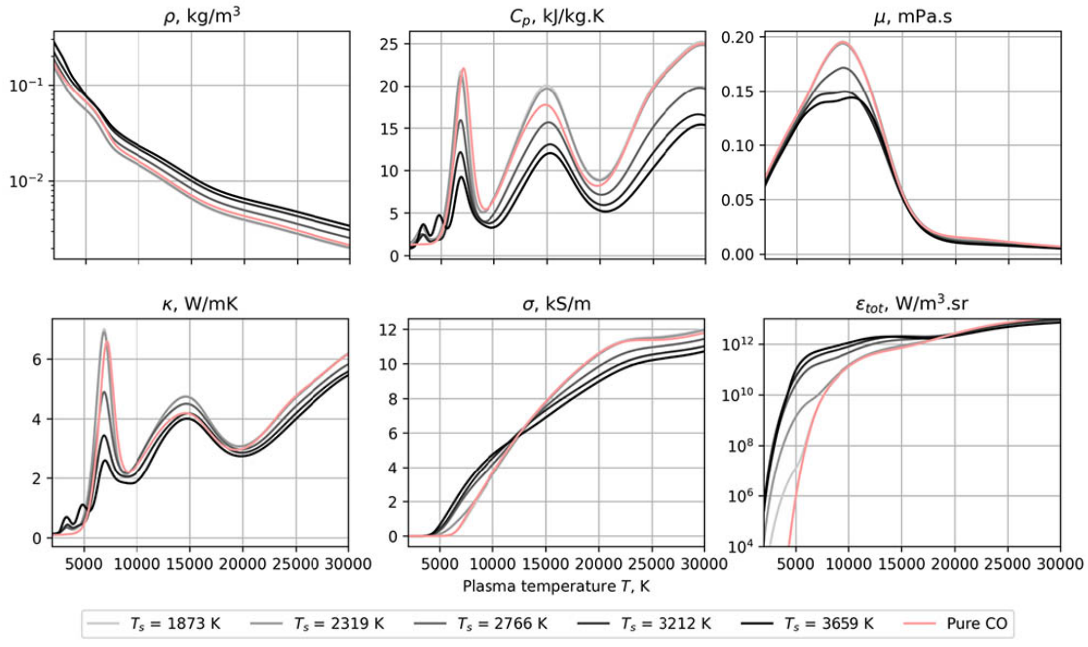

Figure 7—Thermophysical properties of plasmas generated from process gas in DC ilmenite smelting

The degree of reduction and the nickel-to-iron ratio of the feed material determine the alloy product grade and generally the trade-off considers, nickel recovery, slag properties (especially for low Fe ores), the mass of the metal product, and the grade. A notable feature of ferronickel smelting is the high slag-to-metal ratio, which means that a significant portion of the smelting energy is used to generate the nickel-depleted slag.

In the early 1990s, a DC smelting route for producing unrefined ferronickel from nickel-containing laterite was developed at Mintek (Lagendijk, Jones, 1997). In this process, lateritic material, along with a carbonaceous reducing agent, is fed into the central region of the molten bath in a cylindrical DC arc furnace. The high-intensity arc attachment zone in the DC furnace allows for processing nickel laterites with a wide compositional range, making high-intensity processing of fines a key feature of this technology. The DC arc efficiently attracts fines into the smelting zone, where high-intensity smelting is maintained through power-to-feed balance.

Traditional ferronickel smelting in rectangular furnaces also evolved to use arc smelting but with what is described as a shielded arc operation. These operations manage feed cavity formation around the electrodes using multiple feed zones and experience. The shift to high-voltage operation was driven by the need to increase smelting intensity, which was limited in immersed mode (Matyas et al., 1993). The transition to open-arc (high-voltage) operation significantly enhanced smelting intensity for ferronickel smelters who opted for this type of operation. DC smelting represents a high-intensity version of current technology, offering an alternative flowsheet with direct smelting of hot, prereduced fine calcine. This approach reduces electrical energy requirements and offers a high intensity smelting unit. As is the case for ilmenite smelting, DC technology for ferronickel offers a high-intensity alternative to mega-scale six-in-line rectangular furnaces, but the metallurgical basis is the same. The single-electrode design of the DC furnace is mechanically less complex while providing intense processing capabilities with proven capacity to pull fines into the high intensity arc zone.

For the ferronickel case, FactSage simulations were performed based on information by Lagendijk and Jones (1997). The composition of the nickel laterite fines (1.96% NiO) and charcoal given in aforementioned paper was used as is. The feed used in simulations was 100 kg ore, with 5 kg of charcoal. The amount of charcoal was adjusted slightly from the paper to match the simulated composition of metal with that in the paper, which in this case, was 23.3% Ni, condition D5 from Lagendijk and Jones (1997). Simulations were run from 1873 K to the vaporisation temperature of 3646 K with the same step size as for other simulations.

For calculation of the plasma properties the minplascalc species set included Al, C, Ca, Cr, Fe, H, Mg, Mn, Ni, O, Si, Al^+, C^+, Ca^+, Cr^+, Fe^+, H^+, Mg^+, Mn^+, Ni^+, O^+, Si^+, Al^{2+}, C^{2+}, Ca^{2+}, Cr^{2+}, Fe^{2+}, Mg^{2+}, Mn^{2+}, Ni^{2+}, O^{2+}, Si^{2+}, Al^{3+}, C^{3+}, Ca^{3+}, Cr^{3+}, Fe^{3+}, Mg^{3+}, Mn^{3+},

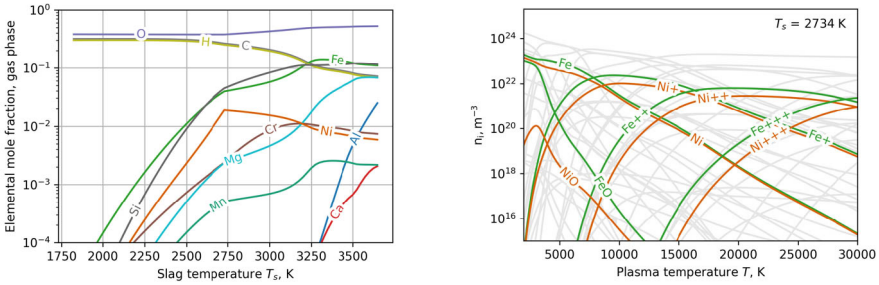

Figure 8—(*l*) Thermochemical calculation of elemental composition of the gas phase during DC ferronickel smelting, (*r*) example plasma species composition calculation at T_s = 2734 K with Fe and Ni species highlighted

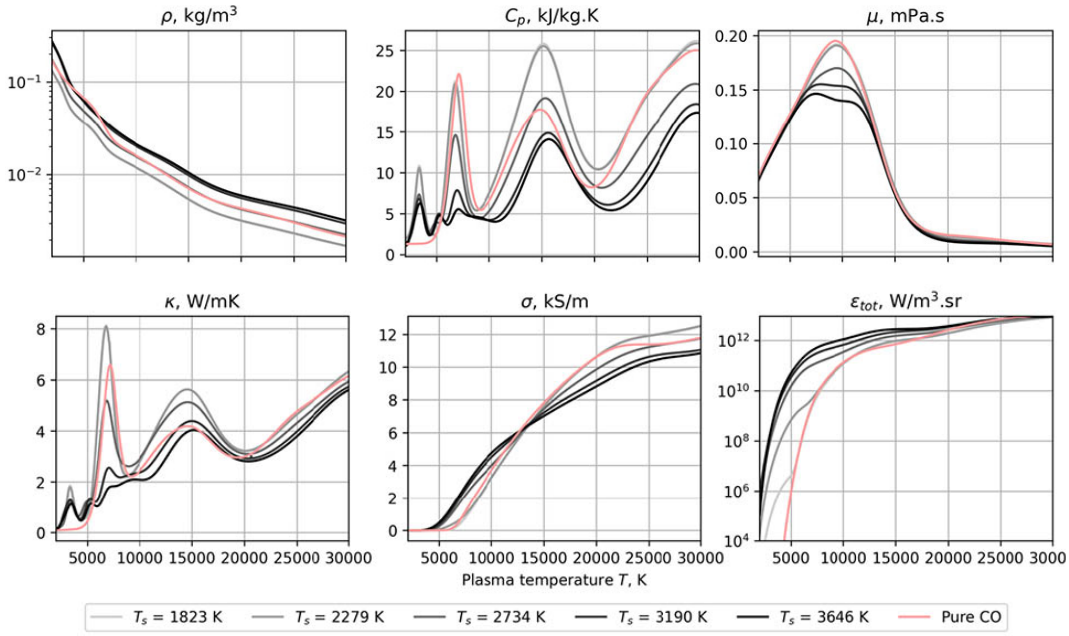

Figure 9—Thermophysical properties of plasmas generated from process gas in DC ferronickel smelting

Ni^{3+}, O^{3+}, Si^{3+}, SiO, NiO, FeO, MgO, CaO, CrO, AlO, CO_2, H_2O, CO, O_2, OH, and H_2. For a selection of slag temperatures over the range shown in Figure 8, the calculations were run between 2000 K and 30000 K at a pressure of one atmosphere. The results are given in Figure 9, with properties of pure CO plasma as a reference.

As another traditional carbothermic oxide smelting process, ferronickel shows somewhat similar behaviour to the previous two cases. For T_s < 2300 K the species present are again predominantly carbon, oxygen, and hydrogen, albeit in different ratios due to the higher moisture content of the feed material in this case. Due to the different ratios, the properties already deviate quite substantially from those of pure CO in this region. For slag temperatures above 2300 K, a familiar pattern is seen where increasing evaporation of metallurgical atomic and molecular species results in drastic changes in the plasma properties, especially for important parameters like σ and ε_{tot}, which have a large influence on the electrical and thermal behaviour of the arc.

ConRoast Platinum Group Metal (PGM) process

The ConRoast process is designed to significantly reduce or eliminate sulphur emissions from sulphide smelting by roasting sulphide-bearing ores prior to smelting (Jones, 2015). This process can be applied to various ores such as nickel sulphides and precious metal sulphides, and is particularly relevant in South Africa's PGM industry where traditional matte smelting is commonly used.

In conventional PGM smelting, PGM-bearing sulphide concentrates are typically melted without the addition of a reductant. Base metal sulphides separate from gangue oxides and PGM concentrate in the matte phase, which is then tapped for further processing – this includes slow cooling, converting, and refining. The ConRoast process offers an alternative approach by roasting (oxidising) the concentrate before the reductive smelting step. The premise is to selectively reduce iron oxide and associated base metal oxides (such as nickel, copper, and cobalt) to the metallic state, and collecting the PGM in the iron-rich alloy. Due to their high affinity for iron, high recoveries can be achieved for PGM. In addition, by removing sulphur before the smelting and converting stages ConRoast effectively eliminates downstream sulphur emissions associated with traditional PGM smelting operations.

The iron alloy produced in the ConRoast process has a higher liquidus temperature than traditional matte. A major contributor to the higher slag liquidus in South African concentrates is the presence of UG2 concentrates, which result from dual production streams of chromite and PGM mining. UG2 concentrates are lower in sulphur and base metals and contain significant residual chromite, which raises the slag's liquidus temperature. Traditional matte smelters manage this 'chrome problem' by increasing the temperature and controlling the chrome content in the feed blend. In the reductive environment of the ConRoast process, chromium predominantly reports to the slag, effectively rejecting chrome during smelting without the adverse effects associated with matte

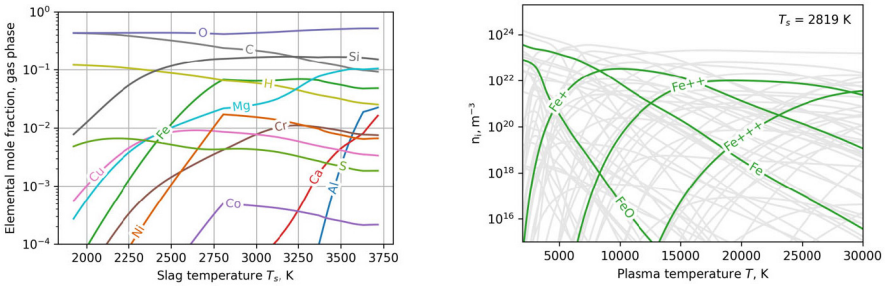

Figure 10—(*l*) Thermochemical calculation of elemental composition of the gas phase during ConRoast DC PGM smelting, (*r*) example plasma species composition calculation at T_s = 2819 K with Fe species highlighted

smelting. The mild reducing conditions required for high PGM and base metal recoveries do not lead to extensive chromium oxide reduction, ensuring that chrome remains in the slag phase.

By roasting the concentrate upfront, most of the sulphur emissions can be contained at a single point. This also allows for hot-feeding the furnace directly from the roaster, which reduces the electrical energy requirement. This process also increases the potential for using a higher ratio of oxide-rich ores in the blend, unlocking access to potentially lower cost feed stocks. DC furnace technology is the preferred embodiment for implementing the ConRoast process due to the ultra-fine nature of PGM ores, where dust losses have a significant economic impact due to the value of the precious metals content. The alloy smelting process provides a high-intensity, efficient smelting method to process PGM-bearing ores without the environmental and health impacts associated with sulphur emissions throughout the plant and addresses several of the typical challenges faced by the industry.

For FactSage simulation of the DC furnace reductive smelting step of the ConRoast process, it was assumed that 100 kg of roasted concentrate reacted with 5 kg of high-grade coke (99.5%C, 0.5% volatiles). The concentrate composition was based on the roasted concentrate analysis with 0.25% S as reported by Jones (2002). Simulations were run from 1923 K to the vaporisation temperature of 3716 K with the same step size as for other simulations.

For calculation of the plasma properties the minplascalc species set included Al, C, Ca, Co, Cr, Cu, Fe, H, Mg, Ni, O, S, Si, Al^+, C^+, Ca^+, Co^+, Cr^+, Cu^+, Fe^+, H^+, Mg^+, O^+, Ni^+, S^+, Si^+, Al^{2+}, C^{2+}, Ca^{2+}, Co^{2+}, Cr^{2+}, Cu^{2+}, Fe^{2+}, Mg^{2+}, Ni^{2+}, O^{2+}, S^{2+}, Si^{2+}, Al^{3+}, C^{3+}, Ca^{3+}, Co^{3+}, Cr^{3+}, Cu^{3+}, Fe^{3+}, Mg^{3+}, O^{3+}, Ni^{3+}, S^{3+}, Si^{3+}, SiS, SiO, NiO, FeO, MgO, CaO, CrO, AlO, CO_2, H_2O, SO_2, CO, O_2, OH, SO, and H_2. For a selection of slag temperatures over the range shown in Figure 10, the calculations were run between 2000 K and 30000 K at a pressure of one atmosphere. The results are given in Figure 11, with properties of pure CO plasma as a reference.

Due to the presence of sulphur compounds in trace amounts, the ConRoast smelting process generates chemically complex gas phases and resulting plasmas. Despite this, a similar pattern to the previous three cases is observed as T_s increases, with properties initially tracking close to those of pure CO (with the exception of σ and ε_{tot} at low plasma temperatures – silicon evaporation contaminates these plasmas from relatively low slag temperatures and affects these two properties disproportionately). At T_s > 2500 K multiple metallic species begin to evaporate, and this produces a large amount of nonlinearity in the heat capacity and thermal conductivity curves particularly.

Enviroplas zinc recovery process

The Enviroplas process is designed for the treatment of solid waste products from the metallurgical industry without requiring agglomeration before smelting (Abdel-latif, 2002). The process is based on the carbothermic reduction of selected metal oxides in these undesirable by-product materials (e.g., nickel, chrome, and zinc oxides). The smelting step occurs at high temperatures and with the preferred implementation using a DC arc furnace offers a

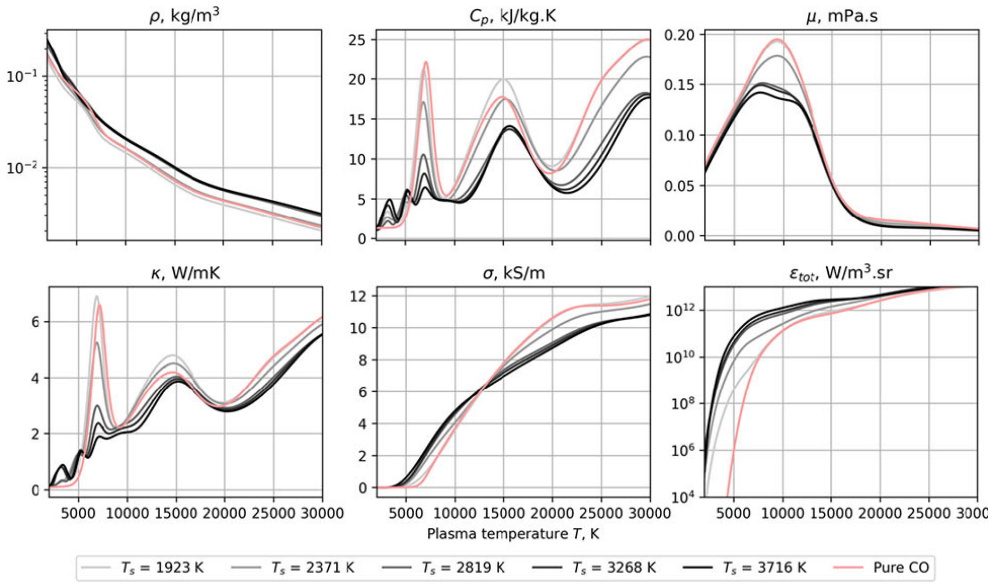

Figure 11—Thermophysical properties of plasmas generated from process gas in ConRoast DC PGM smelting

flexible solution across a wide range of problematic materials. The primary objectives of the process are to produce a non-hazardous disposable slag and, when processing undesirable by-products from stainless steel operations (e.g., AOD dust or similar), to recover chromium and nickel into a crude ferroalloy. Both the metal and slag are tapped from the furnace in liquid form.

For materia ls with high zinc content, such as lead blast furnace slags and EAF dusts, the goal is to recover zinc in the furnace off-gas fume while ensuring low levels of zinc in the discard slag. Zinc-rich fume can either be combusted to produce solid ZnO or routed through a condenser to recover metallic zinc, and the slag can be conditioned to achieve the same basicity index as typical blast furnace slag, making it potentially suitable for use as a cement extender when granulated. Both process routes were successfully demonstrated at Mintek in the 1990s.

The DC arc furnace fuming stage for the Enviroplas zinc process was simulated in FactSage based on the parameters and composition for a premelter slag given in the patent for the process (Barcza et al., 1996). It was assumed that 100 kg of premelter slag is fed to the DC furnace with 3 kg coke. The temperature range for simulations was 1723 K to the vaporisation temperature of 3769 K.

For calculation of the plasma properties the minplascalc species set included Al, C, Ca, Cu, Fe, H, Mg, O, Pb, Si, Zn, Al^{+}, C^{+}, Ca^{+}, Cu^{+}, Fe^{+}, H^{+}, Mg^{+}, O^{+}, Pb^{+}, Si^{+}, Zn^{+}, Al^{2+}, C^{2+}, Ca^{2+}, Cu2+, Fe^{2+}, Mg^{2+}, O^{2+}, Pb^{2+}, Si^{2+}, Zn^{2+}, Al^{3+}, C^{3+}, Ca^{3+}, Cu^{3+}, Fe^{3+}, Mg^{3+}, O^{3+}, Pb^{3+}, Si^{3+}, Zn^{3+}, SiO, FeO, MgO, CaO, AlO, PbO, CO_2, H_2O, CO, O_2, OH, and H_2. For a selection of slag temperatures over the range shown in Figure 12, the calculations were run between 2000 K and 30,000 K at a pressure of one atmosphere. The results are given in Figure 13, with properties of pure CO plasma as a reference.

The Enviroplas process intentionally recovers the primary product, zinc, to the gas phase in the DC fuming furnace step. As a result of this, the plasma properties are considerably different to those of pure carbon monoxide across the entire range of T_s. In particular, the electrical conductivity is higher at plasma temperatures between 5000 and 12,000 K, and the radiation emission is stronger by up to four orders of magnitude in the same range. This is likely to have a large effect on arc behaviour and cause some aspects of the electrical and thermal operation of Enviroplas furnaces to be significantly different from traditional smelting processes.

Mintek Thermal Magnesium Process (MTMP)

The thermal production of magnesium at atmospheric pressure was first demonstrated in the late 1980s, with initial test work conducted in a DC arc furnace at a scale of 50 kVA to 100 kVA. This work paved the way for the development of the Mintek Thermal Magnesium Process (Abdel-latif, 2011). Mintek's use of a DC open-arc furnace to produce magnesium vapor allows for operation at temperatures of 1700°C or higher. These elevated temperatures provide a broader selection of slag compositions and feed materials. Operating at atmospheric pressure, instead of under a vacuum as required by conventional magnesium production processes, enables continuous or semi-continuous operation and the possibility of scaling up beyond the 10 MW batch units typical of traditional

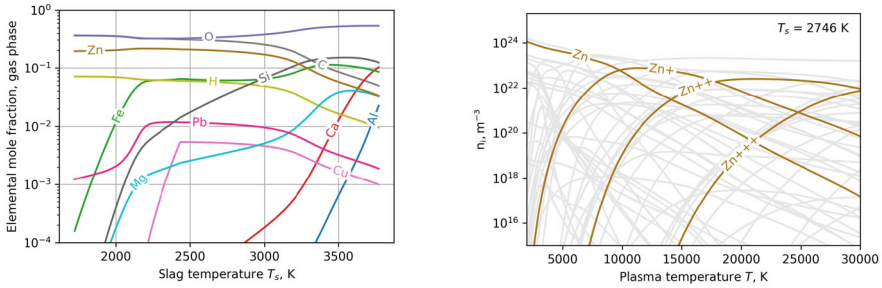

Figure 12—(*l*) Thermochemical calculation of elemental composition of the gas phase during Enviroplas DC zinc smelting, (*r*) example plasma species composition calculation at T_s = 2746 K with Zn species highlighted

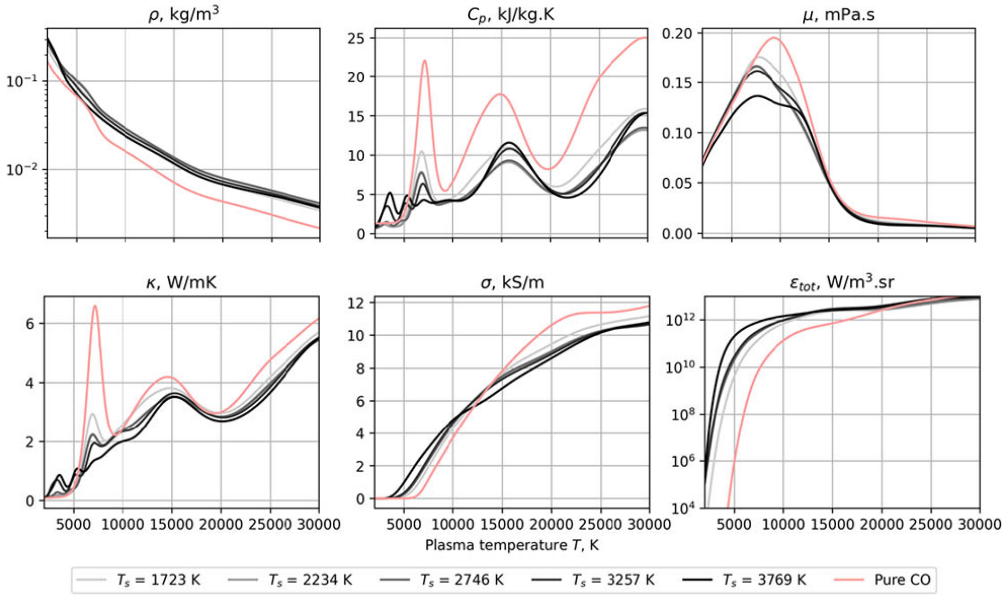

Figure 13—Thermophysical properties of plasmas generated from process gas in Enviroplas DC zinc smelting

methods. By avoiding the use of vacuum conditions, the MTMP reduces the risk of air leakage and the subsequent reoxidation of magnesium.

The process involves the smelting of calcined dolomite in the presence of ferrosilicon at atmospheric pressure. The MTMP is not limited by the electrical properties of the slag, allowing the furnace to operate at relatively high voltages. The volatilised magnesium is captured as liquid metal in a surface condenser unit, which allows for periodic tapping of crude magnesium. The ability to operate under atmospheric pressure facilitates continuous (or semi-continuous) operation in large-scale facilities. The MTMP has been demonstrated on a 1 MW scale, producing high-purity magnesium metal in continuous operation with periodic online cleaning. The DC magnesium process is distinct in that the atmosphere of the sealed furnace is carefully controlled to minimise oxygen in the system. While the Enviroplas process, used for zinc fuming, also operates with metallic vapor, it does not require the same level of sealing and oxygen evacuation as is necessary for magnesium smelting.

The thermochemical simulations for the MTMP were carried out in FactSage based on compositions and parameters stated in the original process patent (Barcza, Schoukens, 1986). The feed consists of 77% calcined dolomite, 13% FeSi, and 10% Al_2O_3. Simulations were carried out assuming the pressure of 85 kPa stated in the patent, and the mole fraction of Ar gas was 0.5 at the normal operating temperature. Simulations were run from 1923 K to the vaporisation temperature of 3873 K with the same step size as for other simulations.

For calculation of the plasma properties the minplascalc species set included Al, Ar, C, Ca, Fe, Mg, O, Si, Al^+, Ar^+, C^+, Ca^+, Fe^+, Mg^+, O^+, Si^+, Al2+, Ar^{2+}, C^{2+}, Ca2+, Fe^{2+}, Mg^{2+}, O^{2+}, Si^{2+}, Al^{2+}, Ar^{2+}, C^{3+}, Ca^{3+}, Fe^{3+}, Mg^{3+}, O^{3+}, Si^{3+}, SiO, FeO, MgO, CaO, AlO, CO, and O_2. For a selection of slag temperatures over the range shown in Figure 14, the calculations were run between 2000 K and 30,000 K at a pressure of one atmosphere. The results are given in Figure 15, with properties of pure CO plasma as a reference.

As mentioned, the MTMP is a somewhat unique case. Similarly to Enviroplas, it recovers its primary product – magnesium – as a vapour in the gas phase. Unlike any of the preceding cases it uses a metallic reductant, which generates no additional gas from the reduction reactions, and argon is used as an inert carrier gas. The gas phase composition is therefore completely different to CO across the entire range of slag temperatures, and the resulting plasma properties show this clearly. There is also not much variation in the properties over the range of T_s, which is likely due to the dominating effect of magnesium, which is present in large fractions. Electrical conductivity between 3000 and 12,000 K is extremely high, as is the total emission coefficient. Arcs in MTMP furnaces are therefore likely to operate very differently indeed, compared to traditional carbothermic smelting processes.

Open-access data set

The raw data used to produce the graphs in the aforementioned is available online (Reynolds, 2024). This data set includes the elemental gas-phase compositions at different process slag

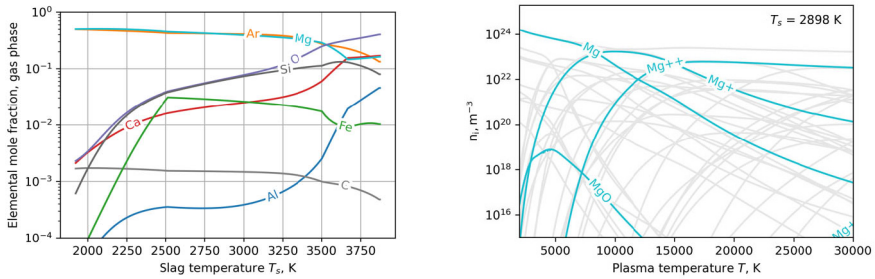

Figure 14—(*l*) Thermochemical calculation of elemental composition of the gas phase during MTMP DC magnesium smelting, (*r*) example plasma species composition calculation at T_s = 2898 K with Mg species highlighted

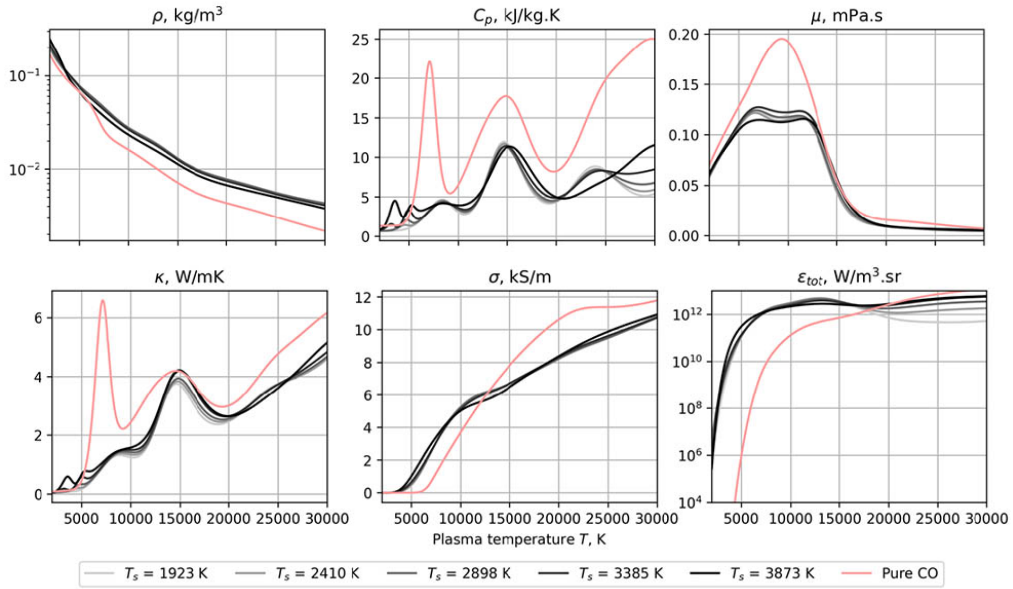

Figure 15—Thermophysical properties of plasmas generated from process gas in MTMP DC magnesium smelting

temperatures T_s calculated using FactSage 8.3, and plasma compositions and properties as a function of plasma temperature T calculated using minplascalc.

Conclusions

As the pyrometallurgy industry advances toward more sustainable processing, large step changes in the design and operation of established unit operations such as DC arc furnaces are expected. These may include variations such as novel ore pretreatment technologies, alternative reductants, energy recovery systems, and complex secondary raw materials such as urban and electronic wastes. In this context, digital modelling tools for rapid prototyping and optimisation will be critical to support effective and agile decision-making; plasma properties calculation methods and workflows such as those described here can potentially be of some value in this ecosystem.

A review of DC arc furnace projects conducted at Mintek over the past five decades has shown how plasma calculations can provide new ways to look at the thermal and electrical behaviour of processes, and by linking such calculations forward into arc models it is likely that even more case-specific insight can be gained in the future. The authors trust that these results have demonstrated that plasma soup truly can be good for the arc furnace pyrometallurgist's soul.

Acknowledgements

This paper is published with the permission of Mintek. The authors acknowledge the Centre for High Performance Computing (CHPC), South Africa, for providing computational resources to this research project.

References

Abdel-latif, M.A. 2011. Review of the development work on the Mintek Thermal Magnesium Process (MTMP). *Journal of the Southern African Institute of Mining and Metallurgy,* vol. 111, no. 6, pp. 393–399.

Abdel-latif, M.A. 2002. Fundamentals of zinc recovery from metallurgical wastes in the Enviroplas process. *Minerals Engineering*, vol. 15, pp. 945–952. https://doi.org/10.1016/S0892-6875(02)00133-4

Adamo, C., Barone, V. 1999. Toward reliable density functional methods without adjustable parameters: The PBE0 model. *The Journal of Chemical Physics.* vol. 110, pp. 6158–6170. https://doi.org/10.1063/1.478522

Balabanov, N.B., Peterson, K.A. 2005. Systematically convergent basis sets for transition metals. I. All-electron correlation consistent basis sets for the 3d elements Sc–Zn. *The Journal of Chemical Physics.* vol. 123, no. 064107. https://doi.org/10.1063/1.1998907

Bale, C.W., Bélisle, E., Chartrand, P., Decterov, S.A., Eriksson, G., Gheribi, A.E., Hack, K., Jung, I.-H., Kang, Y.-B., Melançon, J., Pelton, A.D., Petersen, S., Robelin, C., Sangster, J., Spencer, P., Van Ende, M.-A. 2016. FactSage thermochemical software and databases, 2010–2016. *Calphad 54*, pp. 35–53. https://doi.org/10.1016/j.calphad.2016.05.002

Barcza, N.A. 1986. The development of large-scale thermal plasma systems. *Journal of the South African Institute of Mining and Metallurgy*, vol. 86, no. 8, pp. 317–333.

Barcza, N.A., Curr, T.R., Jones, R.T. 1990. Metallurgy of open-bath plasma processes. *Pure and Applied Chemistry*. vol. 62, pp. 1761–1772. https://doi.org/10.1351/pac199062091761

Barcza, N.A., Schoukens, A.F.S. 1986. The thermal production of magnesium. South African Patent Application no. 867102.

Barcza, N.A., Schoukens, A.F.S., Denton, G.M. 1996. The processing of zinc bearing materials. South African Patent no. 95/4963.

Boulos, M.I., Fauchais, P., Pfender, E. 1994. Thermal Plasmas: Fundamentals and Applications. Plenum Press, New York, USA.

Bowman, B., Krüger, K. 2009. Arc Furnace Physics. Verlag Stahleisen GmbH, Düsseldorf, Germany.

Carbone, E., Graef, W., Hagelaar, G., Boer, D., Hopkins, M.M., Stephens, J.C., Yee, B.T., Pancheshnyi, S., Van Dijk, J., Pitchford, L. 2021. Data Needs for Modeling Low-Temperature Non-Equilibrium Plasmas: The LXCat Project, History, Perspectives and a Tutorial. Atoms 9, 16. https://doi.org/10.3390/atoms9010016

Chapman, S., Cowling, T.G. 1990. The Mathematical Theory of Non-uniform Gases: An Account of the Kinetic Theory of Viscosity, Thermal Conduction and Diffusion in Gases, Cambridge Mathematical Library. Cambridge University Press.

Denton, G.M., Schoukens, A.F.S. 1993. The production of high titania slag from ilmenite. South African Patent Application no. 935072.

Devoto, R.S. 1967. Transport Coefficients of Partially Ionized Argon. *Physics of Fluids,* vol. 10, no. 2, pp. 354–364. https://doi.org/10.1063/1.1762115

Devoto, R.S. 1966. Transport Properties of Ionized Monatomic Gases. *Physics of Fluids,* vol. 9, no. 6, pp. 1230–1240. https://doi.org/10.1063/1.1761825

Feller, D. 1996. The role of databases in support of computational chemistry calculations. *Journal of Computational Chemistry* vol. 17, pp. 1571–1586. https://doi.org/10.1002/(SICI)1096-987X(199610)17:13<1571::AID-JCC9>3.0.CO;2-P

Frisch, M.J., Trucks, G.W., Schlegel, H.B., Scuseria, G.E., Robb, M.A., Cheeseman, J.R., Scalmani, G., Barone, V., Petersson, G.A., Nakatsuji, H., Li, X., Caricato, M., Marenich, A.V., Bloino, J., Janesko, B.G., Gomperts, R., Mennucci, B., Hratchian, H.P., Ortiz, J.V., Izmaylov, A.F., Sonnenberg, J.L., Williams-Young, D., Ding, F., Lipparini, F., Egidi, F., Goings, J., Peng, B., Petrone, A., Henderson, T., Ranasinghe, D., Zakrzewski, V.G., Gao, J., Rega, N., Zheng, G., Liang, W., Hada, M., Ehara, M., Toyota, K., Fukuda, R., Hasegawa, J., Ishida, M., Nakajima, T., Honda, Y., Kitao, O., Nakai, H., Vreven, T., Throssell, K., Montgomery, J.A., Jr., Peralta, J.E., Ogliaro, F., Bearpark, M.J., Heyd, J.J., Brothers, E.N., Kudin, K.N., Staroverov, V.N., Keith, T.A., Kobayashi, R., Normand, J., Raghavachari, K., Rendell, A.P., Burant, J.C., Iyengar, S.S., Tomasi, J., Cossi, M., Millam, J.M., Klene, M., Adamo, C., Cammi, R., Ochterski, J.W., Martin, R.L., Morokuma, K., Farkas, O., Foresman, J.B., Fox, D.J. 2016. Gaussian 16 Revision C.01.

Geldenhuys, I.J. 2017. The Exact Art and Subtle Science of DC Smelting: Practical Perspectives on the Hot Zone. *JOM 69*, pp. 343–350. https://doi.org/10.1007/s11837-016-2171-z

Geldenhuys, I.J. 2013. Aspects of DC chromite smelting at Mintek - an overview, in: Efficient Technologies in Ferroalloy Industry: *Proceedings of the Thirteenth International Ferroalloys Congress, International Ferroalloys Congress.* Presented at the 13th International Ferroalloys Congress, Public Association INFACON XIII, Almaty, Kazakhstan, pp. 31–47.

Geldenhuys, I.J., Akdogan, G., Reynolds, Q.G. 2021. Towards sustainable processing of vanadium-bearing titaniferous magnetite deposits - an overview of barriers and opportunities, in: *International Minerals Processing Congress*. Presented at the IMPC 2020: XXX International Mineral Processing Congress, The Southern African Institute of Mining and Metallurgy, Cape Town, South Africa, pp. 2566–2581.

Griem, H.R. 1964. Plasma Spectroscopy. McGraw-Hill.

Haraldsson, H., Tesfahunegn, Y.A., Tangstad, M., Sævarsdóttir, G.A. 2021. Modelling of Electric Arcs for Industrial Applications, a Review. SSRN Electron. J. https://doi.org/10.2139/ssrn.3927158

Herzberg, G. 1945. Infrared and Raman Spectra of Polyatomic Molecules, Molecular spectra and molecular structure. Van Nostrand.

Hill, J.G., Peterson, K.A. 2017. Gaussian basis sets for use in correlated molecular calculations. XI. Pseudopotential-based and all-electron relativistic basis sets for alkali metal (K–Fr) and alkaline earth (Ca–Ra) elements. *Journal of Chemical Physics*. vol. 147, no. 244106. https://doi.org/10.1063/1.5010587

Howell, J.R., Mengüç, M.P., Daun, K., Siegel, R. 2020. Thermal Radiation Heat Transfer, 7th ed. CRC Press, Seventh edition. | Boca Raton : CRC Press, 2021. | Revised edition of: Thermal radiation heat transfer / John R. Howell, M. Pinar Mengüç, Robert Siegel. Sixth edition. 2015. https://doi.org/10.1201/9780429327308

Johnson, R. 2022. Computational Chemistry Comparison and Benchmark Database, NIST Standard Reference Database 101. https://doi.org/10.18434/T47C7Z

Jones R.T. 2015. Fundamental aspects of alloys melting in a DC arc furnace (Ph. D.). University of the Witwatersrand, Johannesburg.

Jones R.T. 2002. ConRoast: DC arc smelting of dead-roasted sulphide concentrates, in: Sulfide Smelting '02. Presented at the *Third International Sulfide Smelting Symposium, TMS Annual Meeting*, Seattle, Washington, USA, p. 22 (Mintek Paper no. 8527).

Jones, R.T., Curr, T.R. 2006. Pyrometallurgy at Mintek, in: Southern African Pyrometallurgy 2006. Presented at the Southern African Pyrometallurgy 2006, *The South African Institute of Mining and Metallurgy*, Johannesburg, South Africa, pp. 127–150.

Kendall, R.A., Dunning, T.H., Harrison, R.J. 1992. Electron affinities of the first-row atoms revisited. Systematic basis sets and wave functions. *Journal of Chemical Physics*, vol. 96, pp. 6796–6806. https://doi.org/10.1063/1.462569

Kramida, A., Ralchenko, Y. 1999. NIST Atomic Spectra Database, NIST Standard Reference Database 78. https://doi.org/10.18434/T4W30F

Lagendijk H., Jones R.T. 1997. Production of ferronickel from nickel laterites in a DC-arc furnace, in: Nickel-Cobalt 97. Presented at the *36th Annual Conference of Metallurgists*, Sudbury, Canada, pp. 151–162.

Laricchiuta, A., Colonna, G., Bruno, D., Celiberto, R., Gorse, C., Pirani, F., Capitelli, M. 2007. Classical transport collision integrals for a Lennard-Jones like phenomenological model potential. *Chemical Physics Letters,* vol. 445, pp. 133–139. https://doi.org/10.1016/j.cplett.2007.07.097

Linstrom, P., 1997. NIST Chemistry WebBook, NIST Standard Reference Database 69. https://doi.org/10.18434/T4D303

Makgoale, T., Bogaers, A., Zietsman, J., Akdogan, G. 2021. Momentum Transfer from Arc to Slag Bath in a DC Ilmenite Smelting Furnace: A Computational Analysis. *JOM 73*, pp. 2682–2697. https://doi.org/10.1007/s11837-021-04792-x

Matyas, A., Francki, R.C., Donaldson, K.M., Wasmund, B. 1993. Application of new technology in the design of high-power electric smelting furnaces. *CIM Bulletin,* vol. 86, pp. 92–99.

McQuarrie, D.A. 1973. Statistical Mechanics, Harper's chemistry series. Harper and Row.

Metz, B., Stoll, H., Dolg, M. 2000. Small-core multiconfiguration-Dirac–Hartree–Fock-adjusted pseudopotentials for post-d main group elements: Application to PbH and PbO. *Journal of Chemical Physics*, vol. 113, pp. 2563–2569. https://doi.org/10.1063/1.1305880

Peterson, K.A. 2003. Systematically convergent basis sets with relativistic pseudopotentials. I. Correlation consistent basis sets for the post- d group 13–15 elements. *Journal of Chemical Physics*, vol. 119, pp. 11099–11112. https://doi.org/10.1063/1.1622923

Pistorius, P.C. 2008. Ilmenite smelting: the basics. *The Journal of the Southern African Institute of Minining and Metallurgy,* vol. 108, pp. 35–43.

Prascher, B.P., Woon, D.E., Peterson, K.A., Dunning, T.H., Wilson, A.K. 2011. Gaussian basis sets for use in correlated molecular calculations. VII. Valence, core-valence, and scalar relativistic basis sets for Li, Be, Na, and Mg. *Theoretical Chemistry Accounts,* vol. 128, pp. 69–82. https://doi.org/10.1007/s00214-010-0764-0

Pritchard, B.P., Altarawy, D., Didier, B., Gibson, T.D., Windus, T.L. 2019. New Basis Set Exchange: An Open, Up-to-Date Resource for the Molecular Sciences Community. *Journal of Chemical Information and Modeling*, vol. 59, pp. 4814–4820. https://doi.org/10.1021/acs.jcim.9b00725

Rapp, D., Francis, W.E. 1962. Charge Exchange between Gaseous Ions and Atoms. *Journal of Chemical Physics*. vol. 37, pp. 2631–2645. https://doi.org/10.1063/1.1733066

Reynolds, Q.G. 2024. Composition and thermophysical properties of metallurgical plasmas - LTE calculations (1.0.0) [Data set]. https://doi.org/10.5281/zenodo.13337769

Reynolds, Q.G. 2018. Influence of the power supply on the behaviour of DC plasma arcs - a modelling study. *J. South. Afr. Inst. Min. Metall*. vol. 118, no. 6, pp. 655–660. http://dx.doi.org/10.17159/2411-9717/2018/v118n6a14

Reynolds, Q.G., Jones, R.T., Reddy, B.D. 2010. Mathematical and computational modelling of the dynamic behaviour of direct current plasma arcs. *Journal of the Southern African Institute of Mining and Met*allurgy, vol. 110, no. 12, pp. 733–742.

Reynolds, Q.G., Sandrock, C. 2024. minplascalc (commit 967faf3), https://github.com/quinnreynolds/minplascalc.

Richardson, A.S. 2019. NRL Plasma Formulary. United States Naval Research Laboratory, Washington D.C., United States of America.

Schuchardt, K.L., Didier, B.T., Elsethagen, T., Sun, L., Gurumoorthi, V., Chase, J., Li, J., Windus, T.L. 2007. Basis Set Exchange: A Community Database for Computational Sciences. *Journal of Chemical Information and Modeling*. vol. 47, pp. 1045–1052. https://doi.org/10.1021/ci600510j

Smirnov, B.M. 1971. The Classical Theory of Resonance Charge Exchange. *JETP 32*, pp. 670–672.

Stewart, J.C., Pyatt, K.D., Jr. 1966. Lowering of Ionization Potentials in Plasmas. *Astrophysical Journal,* vol. 144, p. 1203. https://doi.org/10.1086/148714

Woon, D.E., Dunning, T.H. 1993. Gaussian basis sets for use in correlated molecular calculations. III. The atoms aluminum through argon. *Journal of Chemical Physics,* vol. 98, no. 2, pp. 1358–1371. https://doi.org/10.1063/1.464303

Yang, A., Liu, Y., Zhong, L., Wang, X., Niu, C., Rong, M., Han, G., Zhang, Y., Lu, Y., Wu, Y. 2016. Thermodynamic Properties and Transport Coefficients of CO_2–Cu Thermal Plasmas. *Plasma Chemistry and Plasma Processing,* vol. 36, pp. 1141–1160. https://doi.org/10.1007/s11090-016-9709-2 ◆